RESEARCH ARTICLE | JUNE 06 2023

A 20 A bipolar current source with 140 μA noise over 100 kHz bandwidth

M. Zhao ; A. Restelli ; J. Tao ; Q. Liang ; I. B. Spielman

AIP Advances 13, 065309 (2023)
https://doi.org/10.1063/5.0138145
CHORUS

A 20 A bipolar current source with 140 μA noise over 100 kHz bandwidth

Cite as: AIP Advances 13, 065309 (2023); doi: 10.1063/5.0138145
Submitted: 8 December 2022 • Accepted: 19 May 2023 •
Published Online: 6 June 2023

M. Zhao,[1,a] A. Restelli,[1,b] J. Tao,[1] Q. Liang,[1,2] and I. B. Spielman[1,c]

AFFILIATIONS

[1]Joint Quantum Institute, University of Maryland and the National Institute of Standards and Technology, College Park, Maryland 20742, USA
[2]Department of Physics and Astronomy, Purdue University, West Lafayette, IN 47907, USA

[a]Authors to whom correspondence should be addressed: zmshum@umd.edu
[b]arestell@umd.edu
[c]spielman@umd.edu

ABSTRACT

The precise control of direct current (dc) magnetic fields is crucial in a wide range of experimental platforms, from ultracold quantum gases and nuclear magnetic resonance to precision measurements. In each of these cases, the Zeeman effect causes quantum states to shift in energy as a function of the magnetic field. The development of low-noise current sources is essential because electromagnets are the preferred tool to dynamically control the magnetic field. Here, we describe an ultra-low noise bipolar current source using pairs of complementary n- and p-channel metal–oxide–semiconductor field-effect transistors controlled by zero-drift operational amplifiers. Our source has a 90 kHz inherent bandwidth and provides current from −20 to 20 A with noise (0.1 Hz to 100 kHz) of 140 μA at ±20 A.

I. INTRODUCTION AND MOTIVATION

Magnetic field control is essential in virtually all fields of the physical sciences, and an increasing range of applications has performance requirements that are not provided in commercial products. Here, we focus on applications such as cold quantum gases,[1] precision measurements, and nuclear magnetic resonance (NMR),[2] all of which require high precision ($\lesssim 10\ \mu A/A$) and moderate bandwidth ($\lesssim 100$ kHz) magnetic field control.

These requirements stem from the dependence of energy levels on magnetic field B due to the Zeeman effect[3] that governs the energy difference ΔE between quantum states $|1\rangle$ and $|2\rangle$. It is common to use oscillating electromagnetic fields [with frequency $\omega/(2\pi)$] to resonantly couple such states, for example, driving Rabi oscillations with frequency $\Omega/(2\pi)$. Unwanted changes to B shift the resonance condition, detuning the transition from resonance by $\delta = \Delta E/\hbar - \omega$. Efficient coupling requires a small detuning, i.e., $\Omega \gg \delta$. For example, in the $|F = 1\rangle$ hyperfine ground state of ^{87}Rb, a 1.4 mT magnetic field leads to a $\Delta E \approx h \times 10$ MHz Zeeman splitting between the three constituent m_F sublevels. These states are often coupled by a radio frequency (rf) magnetic field with typical strength of $\Omega/(2\pi) \simeq 1$ kHz. In this situation, a 10 nT magnetic field stability would yield acceptable performance, i.e., ten times smaller than that given by the Rabi frequency.

Although permanent magnets are useful tools for creating magnetic fields, most experiments requiring dynamical magnetic fields use electromagnets created by using coils and currents. Here, we will focus on Helmholtz coil configurations[4] that are useful for creating the homogeneous fields described above. Furthermore, the vector orientation of the magnetic field dictates the coupling strength, implying the need for bipolar supplies for complete control.

Our specific application requires magnetic fields in a ±6 mT range with a ≈10 kHz bandwidth, which, for our coil geometry, implies the need for a bipolar supply with currents in the range of ±20 A. The commercially available Kepco BOP series is a bipolar power supply with low noise and high bandwidth but not ultra-low noise;[5] its typical noise in the current mode is $\lesssim$0.5 mA with a contribution of 60 Hz line noise at the part-per-thousand level.

We met or exceeded these requirements by constructing a bipolar current source with −20 to 20 A range, below 200 μA noise,

and with ≈100 kHz bandwidth. We quantified its performance by using three different measurements: by directly detecting the electric current, by observing the magnetic field, and with spectroscopy of an atomic Bose–Einstein condensate (BEC). Briefly stated, our supply's noise is just 140 μA at 20 A with 90 μA per hour long-term drift. Although the current bandwidth is 89.7 kHz, our 210 μH coils reduce the magnetic field bandwidth to 9 kHz.

Stable low-noise current sensing is a key element for achieving our target current stability. Sense resistors and non-contact fluxgate or Hall-effect-based sensors are typical devices for measuring electric current. The first two have excellent low-noise performance; however, because the bandwidth of fluxgate-based sensors is typically below 10 kHz, we used a sense resistor. In addition, non-contact magnetic field-based sensors can be susceptible to changes in the laboratory magnetic field. We selected a resistor with a small temperature coefficient of resistance (TCR). A small TCR minimizes the change in resistance, and, consequently, in the sensed voltage drop, resulting from any change in the temperature. To further improve stability, we mounted it to a water-cooled cold plate, reducing the sensitivity to changes in the environmental temperature as well as Joule heating.

Two straightforward solutions for generating currents in the ±20 A range rely on either metal–oxide–semiconductor field-effect transistors (MOSFET)[6] or monolithic high-current operational amplifiers (opamps).[7] Owing to the large input offset drift of high-current opamps as well as challenges with proper thermal management, we opted for parallel MOSFETs. Because MOSFETs can be parallelized, our solution is extendable to larger or smaller current ranges depending upon the application.

This paper is organized as follows: In Sec. II, we discuss the circuit design. In Sec. III, we quantify the performance of the circuit by measuring its response on the electric current, magnetic field, and magnetic resonance. We conclude in Sec. IV and comment on lessons learned.

II. CIRCUIT DESCRIPTION

The circuit has three high-level modules depicted in Fig. 1: current sensing module, feedback module, and current generation module. In the current sensing module, a sense resistor transduces the load current to a voltage. The feedback module uses an opamp-based proportional-integral (PI) servo to maintain the sensed voltage at a target value. Finally, the output of the feedback module is used to govern the MOSFETs' gate voltage, thereby determining the current through the load.

A. Current sensing

The high power sense resistor R_s in Fig. 1 is a POWERTRON model, SHR 4–3825, with a 0.01 Ω resistance, a TCR of $\pm 5\,\mu\Omega/(\Omega\,\mathrm{K})$, and a 50 W maximum power rating. R_s transduces the electric current I_s to the voltage by $V_s = I_s R_s$, where V_s is the voltage drop across R_s. Larger values of R_s increase the signal, thereby reducing the relative importance of noise and drift from other system components at the price of increased Joule heating causing a larger temperature change. Our choice of $R_s = 0.01\ \Omega$ would have been too large for a system relying on passive cooling alone; however, we mounted it to a water cooling plate [0.01 K/W at 3.78 l per minute (63 ml/s)] to maintain a constant temperature.

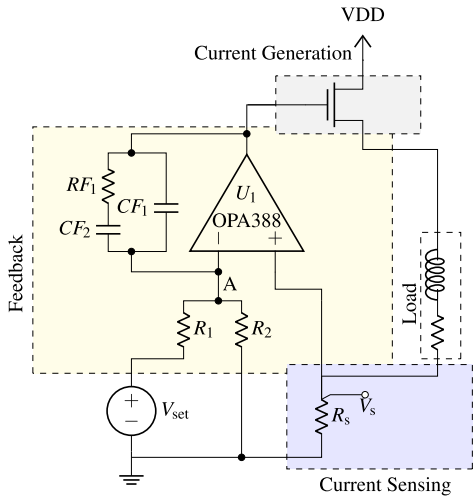

FIG. 1. Schematic of the current sensing of the bipolar current source. The current sensing, feedback, and current generation modules are depicted in purple, yellow, and gray, respectively. The resistor in series with the load inductor models the distributed resistance of the load.

A complete schematic of the circuit is shown in the supplementary material and illustrates two important design details. First, we use a differential amplifier (AD8421) to measure V_s and produce a signal for external monitoring. Second, the internal signal V_s is referenced to an internally defined zero-voltage floating reference node. This avoids uncontrolled voltage drops across parasitic resistances in the return current path.

The sense voltage V_s is the output of this module and provides the input to the feedback module, which is described in the following. In addition, V_s is buffered and amplified by an instrumentation amplifier, providing a monitor output V_m.

B. Feedback

The feedback module controls the amount of current generated by the current generation module and delivered to the load. The feedback module consists of the PI circuit enclosed by the yellow box in Fig. 1. In essence, this circuit compares V_s, the voltage out of the current sensing module, with a fraction $R_2/(R_1 + R_2)$ of the external setpoint V_{set} and then outputs a signal to the current generation module to make these voltages equal.

As shown in Fig. 1, V_s is connected to the positive input terminal of a zero-drift opamp (OPA388). The negative input terminal receives the voltage-divided setpoint $V_{set} \times R_2/(R_1 + R_2)$. Therefore, the setpoint voltage defines the desired output current $I_s = gV_{set}$, with gain $g = R_2/[R_s \times (R_1 + R_2)]$; in our design, $g = 2$ A/V. This gain was chosen so that typical laboratory control voltages in the ±10 V range would yield the desired ±20 A output current.

The properties of the PI loop are governed by the network composed of RF_1, CF_1, and CF_2 with impedance $Z = 1/[sCF_1 + 1/(RF_1 + 1/sCF_2)]$ that link the output and the inverting input of the opamp. Different components would be selected for different loads to optimize the response of the feedback loop. In our implementation, these components are mounted in a socket header to facilitate tuning.

This idealized description omits several properties of real opamps that need to be understood to achieve the desired performance. As shown in the supplementary material, our circuit includes $R_{18} = R_{19}$ and $R_{17} = R_{20}$ to compensate for the bias current of the opamp. Assuming that the bias current of the input terminals is equal, this introduces equal offset voltages to these terminals that vanish in the differential signal. In addition, real opamps have an input offset voltage V_{os} that changes the output current to

$$I_s = gV_{set} + \frac{V_{os}}{R_s}. \quad (1)$$

We see that V_{os} adds an offset to I_s and any drift of V_{os} gives rise to a corresponding drift in I_s, reducing the long-term stability of the current source. It is for this reason that we selected the zero-drift opamp (OPA388) with typical and maximum drifts of 5 and 50 nV/K, respectively.

The output of the feedback module provides the control signal that is the input of the current generation module.

C. Current generation

The current generation module uses *N*-channel MOSFETs (NMOS, IXFN520N075T2) for positive current and *P*-channel MOSFETs (PMOS, IXTN170P10P) for negative current, as shown in Fig. 2. To generate larger currents, these MOSFETs can be parallelized; in our case, two of each type are sufficient to generate currents up to ±20 A. The channel resistance of these MOSFETs is a function of the V_{gs}, the voltage difference between the gate and the source. As a result, we control this resistance and, consequently, the current via the gate voltage. The threshold voltage for nominally identical MOSFETs can differ significantly. As a result, it can be necessary to sort through several MOSFETs to create matched pairs of NMOSs and PMOSs with the same threshold voltage, ensuring that they open simultaneously.

To avoid crossover distortion when the feedback signal passes below the threshold voltage of the MOSFETs, we used a class AB amplifier design.[8,9] MOSFETs have a threshold gate voltage V_{th} below which they do not conduct; the AB amplifier design adds a positive offset voltage to the NMOS gate and a negative offset voltage to the PMOS gate. In our circuit, this is implemented with a pair of non-inverting summing amplifiers (based on LT1363 opamps) that use trim pots to tune these offset voltages close to the threshold voltage of the MOSFET. These components also introduce a suitable gain (of about 10 in our case) on the feedback signal to bring it to the correct level for the MOSFET gates.

The threshold voltages of NMOS and PMOS have opposite polarity, so only one group of MOSFETs will turn on for a specific control signal. For example, when the control signal is positive, the gate voltage of the NMOS and PMOS will be greater than their thresholds, allowing the NMOS to conduct while disabling the PMOS. The LT1363 opamp cannot supply sufficient current to rapidly charge the MOSFET gates. To overcome the bandwidth limit, we added 250 mA BUF634 buffer chips between the LT1363 summing amplifiers and the MOSFETs.

At high current, the inherent negative thermoelectric feedback in MOS transistors should prevent thermal runaway; to further mitigate this concern, we balanced the current load by adding 2.5 mΩ resistors in series with each MOSFET. The ±15 V rails for the MOSFETs are generated by a pair of high-current Agilent 6690 A supplies wired in series and can provide up to 440 A, powering several current supplies with no difficulty.

D. Long-term stability

The two most significant factors that degrade the long-term stability are changes in the sensing resistance R_s (e.g., from a temperature change) and drift in the input offset voltage V_{os} of the main opamp (U_1) in the feedback module. Hence, these effects limit both the precision and accuracy of the circuit.

Our sense resistor has an electrical resistance of 10 mΩ, a thermal resistance of 1.6 K/W, and an expected TCR of 5 $\mu\Omega/(\Omega\,\mathrm{K})$ at 293 K. At the 20 A maximum current, the power dissipation is 4 W, implying a 6.4 K temperature change and a maximum 0.32 $\mu\Omega$ change in resistance in the steady state, which would correspond to a 640 μA change. We note that the TCR of the sense resistor falls to zero at 313 K, making that an ideal operating point. In addition, a

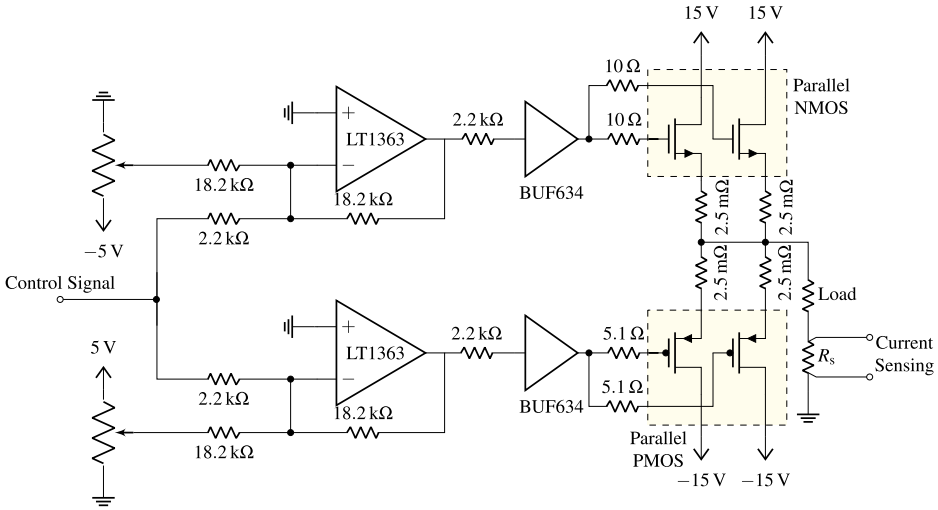

FIG. 2. Schematic of the current generation module. The control signal is input on the left and divided into positive and negative channels (top and bottom, respectively) that control separate banks of NMOS and PMOS transistors before being delivered to the load (far right) and sensed.

10 K temperature change of the control opamp gives a 0.5 μV maximum change in the offset voltage, which would correspond to a 50 μA change in current at ±20 A. We sum these quantities to obtain an upper bound of 690 μA noise at ±20 A for the worst-case drift, dominated by the TCR of the sense resistor.

III. CHARACTERIZATION OF THE CURRENT SOURCE

We characterize the completed current source in three ways. First, we focus on its electrical performance by directly measuring the current noise both with a short circuit and when connected to a realistic test coil. Second, we measured the magnetic field noise in this test coil, and finally, we measured the stability of field-sensitive atomic transitions subject to a field controlled by the source.

A. Electrical characterization

To confirm our desired performance level, we must measure 100 μA on a 10 A background. Observing noise at this scale requires more than 16 bits of digital resolution.

We overcame this technical problem by using a homemade battery-powered instrumentation amplifier with a gain of 54.1 dB and 200 kHz bandwidth, reading the voltage across an additional SHR 4–3825 sense resistor in series with the load. The DC component of the amplified signal was eliminated by a 3 mHz high-pass filter. The remaining signal was read by a signal and spectrum analyzer. We tested the performance of the circuit under two cases: (a) no coils (sense resistor as the load) and completely under battery power; and (b) a 210 μH coil in series with the sense resistor as the load and with the circuit powered by supplies connected to a 110 V AC line.

Figure 3 shows the power spectral density (PSD) measured for drive currents of 20 A (blue) and background noise with the circuit unpowered (orange). Panel (a) shows the data taken with the output terminals short circuited and with the circuit under battery power, while the data in panel (b) were taken with a realistic inductive load and with the circuit powered by 110 V AC. In both cases, engaging the circuit produces a background noise level of about

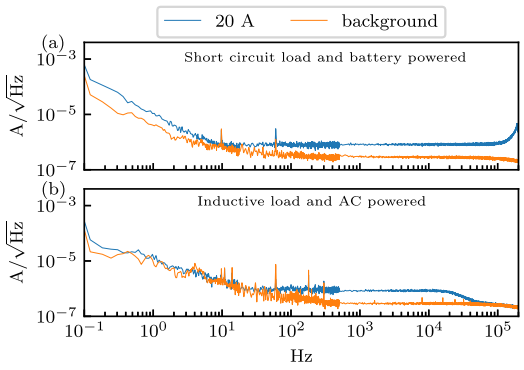

FIG. 3. The 20 A and background electrical noise spectrum is tested under two cases, i.e., (a) no coil and battery powered and (b) coils in the load and AC lines powered. The measurement is performed combining three datasets. From 0.1 to 20 Hz, we used an FFT audio analyzer, while for the remaining frequency range, we combined measurements from a spectrum analyzer performed in two frequency ranges, from 20 to 500 Hz and from 500 Hz to 200 kHz.

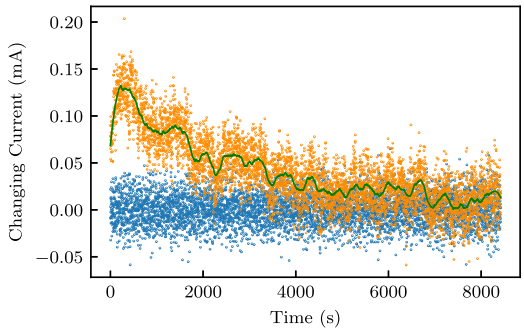

FIG. 4. The long-term drift (orange) of 10 A of the bipolar current source over 8000 s with the filter time constant of 16.6 ms. The blue points show the same data with a 1 min high-pass filter applied. The green line shows the rolling average of the orange points. The drift for the first 4×10^3 s is 90 μA/h. The drift from 4×10^3 to 8×10^3 s is 10 μA/h.

10^{-6} A/$\sqrt{\text{Hz}}$. Because the PI loop is optimized for an inductive load [as shown in Fig. 3(b)], the short-circuit case exhibits a resonance around 200 kHz. In Fig. 3(b), the broadband background-subtracted noise is 0.8 μA/Hz$^{1/2}$ from 10 Hz to 100 kHz. The RMS noise from 0.1 Hz to 100 kHz for cases (a) and (b) are 260 and 140 μA, respectively. Negligible noise difference is found between 20 and −20 A, thereby only 20 A is shown in Fig. 3.

The noise spectrum has peaks at 60 Hz and its harmonics. These peaks persist when the background noise is subtracted, and even when the circuit is completely battery-powered. Additional peaks above 1 kHz appear when the circuit is powered off but connected to AC power. We find that, in the former case, the 60 Hz features result from ground loops introduced by the spectrum analyzer (which is AC powered). We were unable to identify the origin of higher frequency features, but we speculate that a poorly designed switching supply is introducing noise onto our mains.

A second performance metric is the ability of the current source to consistently deliver the commanded current over very long time scales. This long-time behavior is generally characterized by an apparent drift of the current that is not described by a white noise process. In our atomic physics experiments, this drift can be as important as the higher frequency noise performance. Figure 4 plots the change in current on top of a 10 A set point over a multi-hour period, showing a drift of 100 μA per hour. The current is transduced to voltage by an additional SHR 4–3825 sense resistor in series with the load, which was measured by a 7.5-digit multimeter.

In our laboratory,[10] we often use atomic transitions to stroboscopically measure and servo the magnetic field with a feedback time constant of around 1 min. The blue curve shows the same data with a 1 min high-pass filter applied, showing that, in our implementation, long-term drift can be made irrelevant. This, along with the multimeter's internal ≈17 ms time constant, gives a high-frequency noise estimate of 2 μA/Hz$^{1/2}$.

B. Magnetic characterization

In our application, we employ the current source to generate magnetic fields using air-core electromagnets, and in this section, we characterize the associated magnetic field performance. We used a

low-noise fluxgate sensor for the magnetic field measurement; however, its measurement range is ±100 μT. To avoid saturating the fluxgate, we drove independent currents through the anti-Helmholtz coil pair shown in the inset of Fig. 5 to null the magnetic field at the midpoint. We used nominally identical 60-turn coils with 210 μH inductance and 0.1 Ω resistance. The currents were sourced by independent current supplies and we needed slightly different currents in the coils to reach the null point.

We then measured the short-term magnetic field noise for the two cases shown in Fig. 5. Each case is the average over ten measured time sequences captured by an oscilloscope. The orange curve shows the background field noise obtained with the two independent current sources turned off. The blue data show the noise spectrum with 20 A and with the background subtracted. By integrating, we obtain the RMS noise level B_{noise} = 46.0 nT at 20 A from 20 Hz to 1 kHz. As with the current noise, 60 Hz and its harmonics still contribute significantly.

We also used the fluxgate for the current to magnetic field calibration. This was achieved by scanning the current in one coil over a 100 mA range (as large as possible without saturating the fluxgate) with the current in the other coil fixed and obtaining the ratio $\delta B/\delta I$ = 1.147 mT/A. From this, we find the short-term 40 μA noise at 20 A from 20 Hz to 1 kHz.

C. Response time

In our application, we change the magnetic field on the 100 μs time scale. The response time is limited both by the bandwidth of our supply and the inductive time scale of the coils. Therefore, we first measured the current response time and then separately obtained the field response time.

The current response was obtained from the built-in sensing resistor with the same 210 μH coil used in the stability test as the load. The impulse response function for a step from 1.8 to 2.2 A is plotted in Fig. 6(a) showing an ≈5 μs response time. The 10%–90% rise time is 3.9 μs, giving a 3 dB bandwidth of ≈90 kHz.

Our fluxgate sensors are insufficient to measure the field-response time because their bandwidth is less than 1 kHz. Therefore, we constructed a pickup coil to measure the derivative of the magnetic field impulse response function, as shown in green in Fig. 6(b),

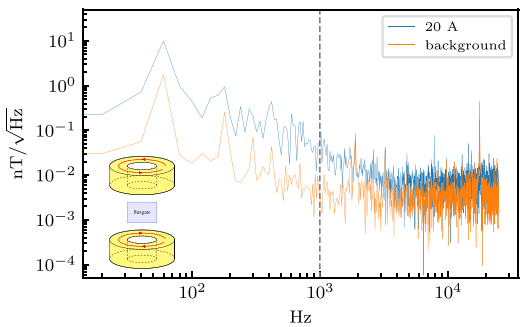

FIG. 5. Short-term noise spectrum for the background magnetic field (orange), and magnetic field at 20 A (blue) over 50 ms with a 5×10^4 s^{-1} sampling rate. The vertical dashed line indicates the bandwidth of the fluxgate. The inset shows the setup of the current stability measurements. The fluxgate is placed at the center of an anti-Helmholtz coil pair.

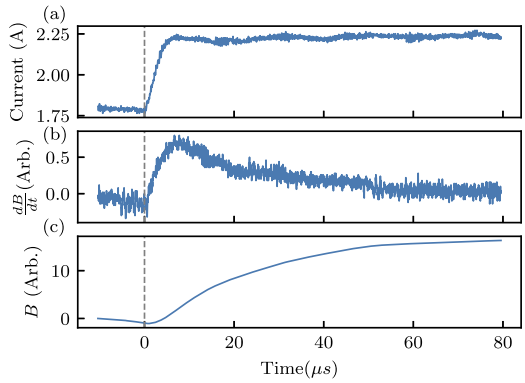

FIG. 6. Response of a current jump from 1.8 to 2.2 A for the bipolar current source with a 210 μH inductive load. (a) The current read from the built-in current monitor. (b) The magnetic field time derivative dB/dt read from a pickup coil. (c) The magnetic field B by the numerical integral of (b). The current rise time is 3.9 μs, and the magnetic field settling time is 39.7 μs. The vertical dashed line indicates the time when the current turns on.

and numerically integrated these data to recover the magnetic field response shown in Fig. 6(c). The magnetic field response exhibits a brief ≈2.5 μs delay followed by a slower, inductively limited, approach to the set point. The 10%–90% rise time is 39.7 μs, giving a 3 dB bandwidth of ≈9 kHz.

D. Transition energy characterization

In our experiments, we use magnetic fields to control atomic energy differences in atomic Bose–Einstein condensates (BECs) via the Zeeman effect. This sensitivity provides a very accurate method for measuring the *in situ* magnetic field stability.

We prepared $N = 1.7 \times 10^5$ atom ^{87}Rb BECs in a crossed optical dipole trap[11] in the $|f = 1, m_F = 1\rangle$ hyperfine ground state. The magnetic field was monitored by driving the field-sensitive ≈6.834 GHz microwave transitions between the $|f = 1, m_F = 1\rangle$ and $|f = 2, m_F = 2\rangle$ states.

The magnetic field was provided by eight separately controlled coils[12] to generate a magnetic field along $\mathbf{e}_z$.

We selected a magnetic field detuned by 440 kHz from resonance and then ramped on the microwaves in 3 ms to a Rabi frequency of about 10 kHz. Then, we swept the magnetic field to the resonance in 30 ms and finally reduced the microwave Rabi frequency $\Omega/(2\pi)$ = 1.5 kHz in 32 ms. After a 60 ms hold time, the microwave field was abruptly turned off. The spin populations N_1 and N_2 in the two hyperfine states were measured following a 10 ms time of flight.

The expected fractional population

$$f_1 \equiv \frac{N_1}{N} = 1 - \frac{1}{1 + \left(\bar{\delta} + \sqrt{1 + \bar{\delta}^2}\right)^2} \tag{2}$$

only depends on the dimensionless detuning $\bar{\delta} = \delta/\Omega$, where δ is the detuning from microwave resonance.

The fractional population f_1 for 150 repetitions of the experiment spanning about 120 min is shown in Fig. 7. The observed standard deviation δf_1 = 0.034 corresponds to a transition frequency

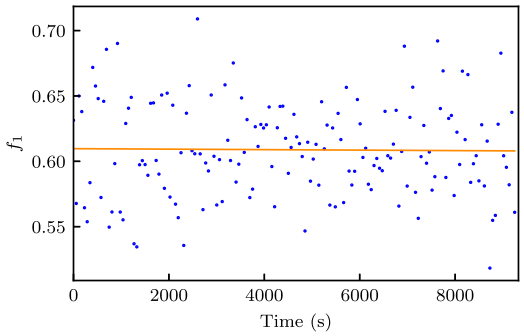

FIG. 7. Fractional population f_1 in $|1,1\rangle$ and $|2,2\rangle$ comprising a microwave-dressed state (blue). The linear fit (orange) has a slope of $-0.7(40) \times 10^{-3}$/h corresponding to a magnetic field drift of $-0.1(6)$ nT/h.

noise, magnetic field, and current noise with standard deviation of 113 Hz, 5.4 nT, and 18 μA, respectively. Since this noise resulted from the noise of eight independent supplies, we estimate the noise for a single supply to be $18/\sqrt{8} = 6.4$ μA. The effective bandwidth of this measurement is approximately equal to the microwave Rabi frequency, and thus, the noise density can be calculated as 165 nA/$\sqrt{\text{Hz}}$ for frequency lower than 1.5 kHz. We note that this is an overestimate of the true noise because it included the statistical and systematic errors associated with detecting and counting the atoms. The long-term drift is estimated to be 0.6 μA/h with an uncertainty of 3.6 μA/h. This estimate omits the uncertainty in the spin population measurements and is, therefore, an upper bound on the supply noise.

IV. CONCLUSION

We developed a highly stable bipolar current source by using parallel MOSFETs controlled by a zero-drift opamp. The current output ranges from −20 to 20 A with short-term noise 140 μA and long-term drift of 90 μA/h of the output current and 0.6 μA/h obtained from atomic spectroscopy.

The current and magnetic field bandwidth is up to 90 and 9 kHz, respectively, for an inductive ≈200 μH coil. Adjustable proportional and integral gain can be tuned for different loads. This bipolar current source could be used for magnetic field control in the cold atom and NMR experiments and other applications requiring bipolar current control.

While this circuit is highly performant, our experience developing it indicates further avenues for improvement. To further eliminate thermal effects, it would be desirable to stabilize the sense resistor around 313 K (for the optimal TCR) and to split the current into more than one resistor (to reduce Joule heating). The coil picks up changing laboratory magnetic fields from DC to >10 MHz and the resulting current is rectified by non-linear circuit elements and then detected by our sense resistor. It would be desirable to strongly filter the output of the current sensing module above the system's closed-loop bandwidth. The installed system picks up additional line noise from the external voltage set point. It would be desirable to include a precision on-board digital to analog converter, connected by optical fiber or high-speed ethernet to break all ground loops.

SUPPLEMENTARY MATERIAL

The complete circuit schematics are included in the supplementary material. We made all our schematic diagrams and printed circuit board layouts available online.[13]

ACKNOWLEDGMENTS

We thank F. Salcés-Carcoba, A. Valdés-Curiel, and E. Fenton for the initial design of the cold-atom apparatus and for considerable construction assistance, and C. J. Billington for designing our vector-tensor coil assembly. The authors thank J. Bienfang, E. Benck, and P. Banner for carefully reading the manuscript. This work was partially supported by the National Institute of Standards and Technology, the National Science Foundation through the Physics Frontier Center at the Joint Quantum Institute (Grant No. PHY-1430094), and the Quantum Leap Challenge Institute for Robust Quantum Simulation (Grant No. OMA-2120757).

AUTHOR DECLARATIONS

Conflict of Interest

The authors have no conflicts to disclose.

Author Contributions

M. Zhao: Conceptualization (equal); Data curation (equal); Formal analysis (equal); Visualization (equal); Writing – original draft (equal); Writing – review & editing (equal). **A. Restelli**: Conceptualization (equal); Data curation (equal); Formal analysis (equal); Visualization (equal); Writing – review & editing (equal). **J. Tao**: Data curation (equal); Writing – review & editing (equal). **Q. Liang**: Data curation (equal). **I. B. Spielman**: Conceptualization (equal); Data curation (equal); Formal analysis (equal); Funding acquisition (equal); Investigation (equal); Resources (equal); Supervision (equal); Writing – original draft (equal); Writing – review & editing (equal).

DATA AVAILABILITY

The data that support the findings of this study are available from the corresponding author upon reasonable request.

REFERENCES

[1] Y.-M. Yang, H.-T. Xie, W.-C. Ji, Y.-F. Wang, W.-Y. Zhang, S. Chen, and X. Jiang, "Ultra-low noise and high bandwidth bipolar current driver for precise magnetic field control," Rev. Sci. Instrum. **90**, 014701 (2019).

[2] J. Koivuniemi, R. Luusalo, and P. Hakonen, "Bipolar programmable current supply for superconducting nuclear magnetic resonance magnets," Rev. Sci. Instrum. **69**, 3418–3425 (1998).

[3]C. J. Foot *et al.*, *Atomic Physics* (Oxford University Press, 2005), Vol. 7.
[4]A. E. Ruark and M. F. Peters, "Helmholtz coils for producing uniform magnetic fields," J. Opt. Soc. Am. **13**, 205–212 (1926).
[5]Certain commercial equipment, instruments, or materials are identified in this paper to specify the experimental procedure adequately. Such identification is neither intended to imply recommendation or endorsement by the National Institute of Standards and Technology nor is it intended to imply that the materials or equipment identified are necessarily the best available for the purpose.
[6]R. Thomas and N. Kjærgaard, "A digital feedback controller for stabilizing large electric currents to the ppm level for Feshbach resonance studies," Rev. Sci. Instrum. **91**, 034705 (2020).
[7]C.-L. Hung, *In Situ Probing of Two-Dimensional Quantum Gases* (The University of Chicago, 2011).
[8]B. Duncan, *High Performance Audio Power Amplifiers* (Elsevier, 1996).
[9]P. Horowitz and W. Hill, *The Art of Electronics* (Cambridge University Press, Cambridge, 2002).
[10]Q.-Y. Liang, D. Trypogeorgos, A. Valdés-Curiel, J. Tao, M. Zhao, and I. B. Spielman, "Coherence and decoherence in the Harper–Hofstadter model," Phys. Rev. Res. **3**, 023058 (2021).
[11]Y.-J. Lin, A. R. Perry, R. L. Compton, I. B. Spielman, and J. V. Porto, "Rapid production of ^{87}Rb Bose–Einstein condensates in a combined magnetic and optical potential," Phys. Rev. A **79**, 063631 (2009).
[12]This coil geometry allows us to fully control the magnetic field vector and its gradient tensor.
[13]JQI, "20 A-bipolar-current-source," https://github.com/JQIamo/20A-bipolar-current-source, 2023.